Supporting Information

Cristino et al. 10.1073/pnas.1219485110

SI Materials and Methods

Animals and Diet. Experiments were performed under institutional approval and according to the guidelines of the institutional ethical code and the Italian (D.L. 116/92) and European (Official Journal of European Community L358/1 12/18/1986) regulations for the care and use of laboratory animals. All mice were maintained on a 12-h light/dark cycle and fed ad libitum. Male mice with spontaneous nonsense mutation of the *ob* gene for leptin (*ob*/*ob*, JAX mouse strain) B6.V-Lep^{ob}/J and WT *ob* gene expressing homozygous siblings of different ages were obtained from breeding *ob* gene heterozygotes, and genotyped with PCR. The pups were housed together with their dam up to weaning and consumed maternal milk only. After weaning, all these animals were fed ad libitum with a standard laboratory regimen (diet SFD TD2018 providing 3.5 Kcal/g as 5.7% fat, 18.9% protein and 57.3% carbohydrate; Harlan Laboratories). Nine-week-old male C57BL/6J mice were made obese by being fed 7 wk of high-fat diet (HFD) (n = 6; diet HFD TD97366 providing 4.7 Kcal/g as 49% fat, 18% protein and 33% carbohydrate; Harlan Laboratories). Lean mice received a standard fat diet (SFD) (n = 6; diet SFD TD2018). Serum leptin levels were determined using commercial sandwich ELISAs (B-Bridge International) in accordance with the manufacturer's instructions.

Male obese (*ob*/*ob* or HFD*)* mice and lean (WT and SFD) littermates were injected with a single dose of recombinant leptin (5 mg/kg in 100 μL saline, i.p.; Sigma Aldrich; n = 6 mice per group) or saline (vehicle n = 6 mice per group). Leptin injection was also combined with administration of leptin receptor antagonist (recombinant mouse leptin antagonist triple mutant, Prospec, Rehovot, Israel; 5 mg/kg in 100 μL saline, i.p.; n = 6 mice per group) or rapamycin (6 mg/kg in 100 μL saline, i.p.; LC Laboratories; n = 6 mice per group) or the cannabinoid receptor type-1 (CB_1) inverse agonist AM251 (AM; 10 mg/kg, i.p.; Tocris; n = 3 mice per group). Leptin was also injected 1 h after administration of anti-leptin or rapamycin. Leptin injections were performed 24 h after food withdrawal and the animals were killed 24 h after ad libitum feeding. For the food intake and plasma cathecolamine and cortisol studies, obese and lean mice were injected with hypocretin-1/orexin-A receptor (OX-A) antagonist (SB-334867; Tocris, 60 mg/kg, i.p., n = 3 mice per group) per se or 2 h before OX injection (Tocris; 40 mg/kg, i.p., n = 3 mice per group).

Immunohistochemistry and Antibodies. Under deep pentobarbital anesthesia (60 mg/kg, i.p.), mice were perfused transcardially with 4% (wt/vol) paraformaldehyde/0.1M phosphate buffer, pH 7.4 (PB) for confocal or light microscopy immunohistochemistry or with 3% (vol/vol) paraformaldehyde/0.5–1% glutaraldehyde in PB for immunoelectron microscopy. Brains destined to immunohistochemistry were cut with a Leica CM3050S cryostat into 10-μm-thick serial sections in the coronal plane, collected in alternate series and processed for immunofluorescence or immunoperoxidase with specific primary antibodies. The following primary antibodies were used: rabbit or guinea pig anti-DAGLα and rabbit anti-serine hydrolase α-β-hydrolase domain 6 (ABHD6) as previously characterized (1, 2), rabbit anti-CB_1R (Calbiochem, Merck), goat anti-OX-A (Santa Cruz Biothechnology), goat antimonoacylglycerol lipase (anti-MAGL) or antimelanin-concentrating hormone (anti-MCH) (Abcam) (range 1:200–1:400), antisynaptophysin, antivesicular GABA transporter (anti-VGAT), antivesicular glutamate transporter 2 (anti-VGluT2) and anti-VGluT1 (Synaptic Systems), rabbit anti-pSTAT3 (Abcam), anti-STAT3 (Santa Cruz Biothechnology), anti-pS6K1 (Cell Signaling Technology), anti-neuropeptide Y (anti-NPY), anti–pro-opiomelanocortin (anti-POMC) (Phoenix Pharmaceutical), anti–α-melanocyte-stimulating hormones (αMSH) (Abcam) (dilution range 1:600–1:1,000). For multiple immunofluorescence for the visualization of puncta apposed to OX neurons, the sections were incubated in a mixture of anti–OX-A antibodies combined with antibodies that recognized diacylglycerol lipase-α (DAGLα) or CB_1R or CB_1R/synaptophysin or CB_1R/VGluT2 or CB_1R/VGAT or MAGL/VGAT or MAGL/VGluT2. Multiple immunofluorescence for the visualization of MCH neurons was performed with a mixture of anti-MCH antibodies and antibodies that recognized CB_1R/VGluT2, CB_1R/VGAT, or CB_1R/synaptophysin (all diluted 1:100–1:300 in donkey serum). Immunofluorescence was revealed by specific Alexa-488 or -546 or -350 secondary donkey anti-IgGs (Invitrogen Life Technology). Controls of specificity of immunolabeling in multiple fluorescence experiments were performed by omission of primary and secondary antibodies or by preadsorbtion of primary antibodies with the respective blocking peptides.

Confocal Imaging and Synaptic Distribution Analysis. Sections through the lateral hypothalamus (LH) were observed with a laser-scanning confocal microscope (LSM510 Meta, Zeiss). Synaptic distribution was analyzed in confocal images stacks using the Metamorph Imaging Software (Leica MetaMorph AF). After identification of individual OX neuron and thresholding, only puncta apposed to OX somata and proximal dendrites were counted. The same procedure was adopted for counting CB_1R/NPY or CB_1R/αMSH axon terminals apposed to OX neurons. Quantification of DAGLα or CB_1R or OX peroxidase-based immunostaining was performed measuring optical density on digital images acquired under constant light illumination and at the same magnification. In each section the optical density zero value was assigned to the background (i.e., a tissue portion devoid of stained cell bodies or fibers). The optical density of DAGLα or CB_1R was evaluated in relation to OX neurons identified in adjacent labeled sections (n = 3 mice and n = 100–120 OX neurons per genotype and diet group).

Preembedding Immunogold Silver-Enhanced Electron Microscopy and Analysis. Sections (50-μm-thick) prepared from the LH of mice with a microslicer (VT1000S; Leica) were dipped in 5% BSA/0.02% saponin (wt/vol) PBS for 30 min and incubated overnight free-floating at +4 °C in a mixture of primary antibodies (anti-CB_1R/anti-DAGLα or anti-OX/anti-CB_1R or anti-OX/anti-DAGLα, diluted with 1% BSA/0.004% saponin in PBS). The sections were incubated for 4 h in the first secondary antibody, diluted in 1% BSA/0.004% saponin/PBS, followed by the first silver enhancement and then by incubation with the second secondary antibody followed by the last silver enhancement. All of the secondary antibodies were conjugated to ultrasmall gold particles <1.0 nm; (Aurion). To prevent loss of labeling during silver enhancement, sections were fixed with 2.5% (wt/vol) glutaraldehyde in PB for 2 h at 4 °C under gentle agitation. Sections were then treated with 0.5% OsO_4 in PB for 10 min at 4 °C, dehydrated in an ascending series of ethanol and propylene oxide and embedded in TAAB 812 resin (TAAB). During dehydration, sections were treated with 1% uranyl acetate in 70% (vol/vol) ethanol for 15 min at 4 °C. Ultrathin (60-nm) sections were collected on Formovar-coated, single- or multiple-slot (50-mesh) grids, and stained with 0.65% lead citrate. Electron micrographs were taken with the transmission electron microscope (TEM) LEO 912AB Zeiss. Additional sections were processed in parallel as negative controls omitting the primary or secondary antibodies or silver enhancer. Moreover, controls of

metal particle size were performed following single vs. double silver enhancement of all secondary antibodies. When amplified by only one step of silver enhancement, metal particles showed a mean diameter of 45.8 ± 12.5 nm (small size) whereas those amplified by a double sequential step of silver-enhancement showed a mean diameter of 92.5 ± 18.6 nm (large size) (Fig. S1 *F*, *G*, and *I*). The relative size distribution of single or double silver-enhanced immunolabeling is shown for CB_1R in Fig. S1*I*.

Preembedding Immunogold Labeling. Double preembedding immunogold labeling was performed on 50-μm vibratome sections through the LH of obese and lean mice. These sections were incubated free-floating overnight at 4 °C with a mixture of primary antibodies (rabbit anti-CB_1R and guinea pig anti-DAGLα or goat anti–OX-A and rabbit anti-CB_1 or goat anti–OX-A and guinea pig anti-DAGLα), all diluted 1:100 in donkey serum blocking solution with 0.02% saponin. The sections were then incubated in a mixture of 10-nm and 6-nm gold-conjugated secondary antibodies (Aurion), diluted 1:30 in donkey serum blocking solution with 0.02% saponin. Sections were then treated with 0.5% OsO_4 in PB for 10 min at 4 °C, dehydrated in an ascending series of ethanol and propylene oxide and embedded in TAAB 812 resin (TAAB). During dehydration, sections were treated with 1% uranyl acetate in 70% ethanol (vol/vol) for 15 min at 4 °C. Ultrathin (60-nm) sections were cut perpendicularly to the surface of 50-μm vibratome sections, collected on Formovar-coated, single- or multiple-slot (50-mesh) grids and stained with 0.65% lead citrate. Electron micrographs were taken with the TEM microscope (LEO 912AB; Zeiss). The TEM observation was limited to series sectioned up to 0.6–0.8 μm depth of preembedded immunolabeled tissue. Additional sections were processed in parallel as controls of reaction by omitting both or one of the primary antibodies from the mixture. No labeling was detected in the control material.

Lipid Extraction and Endocannabinoid Measurement. Tissue samples from the LH were homogenized in 5 vol chloroform/methanol/Tris·HCl 50 mM (2:1:1 by volume) containing 10 pmol of d^8-anandamide and 50 pmol of d^5-2-arachidonoylglycerol (d^5-2-AG). Homogenates were centrifuged at 13,000 × *g* for 16 min (4 °C), the aqueous phase plus debris were collected and four times extracted with 1 vol chloroform. The lipid-containing organic phases were dried and prepurified by open-bed chromatography on silica columns eluted with increasing concentrations of methanol in chloroform. Fractions for anandamide and 2-AG measurements were obtained by eluting the columns with 9:1 (by volume) chloroform/methanol and then directly analyzed by liquid chromatography-atmospheric pressure chemical ionization-mass spectrometry (LC-APCI-MS). LC-APCI-MS analyses were carried out in the selected ion monitoring mode, using *m*/*z* values of 356 and 348 (molecular ions +1 for deuterated and undeuterated anandamide), 384.35 and 379.35 (molecular ions +1 for deuterated and undeuterated 2-AG). Anandamide and 2-AG levels were therefore calculated on the basis of their area ratios with the internal deuterated standard signal areas, their amounts in picomoles normalized per milligram of lipids and compared by ANOVA followed by the post hoc Bonferroni test.

***Preproorexin* mRNA Quantification by RT-PCR Analysis.** Tissue samples from LH were dissected from $n = 3$ animals per group, collected in RNA Later (Invitrogen Life Technology) following the manufacturer's instructions and homogenized in 1.0 mL of TRIzol (Invitrogen). Total RNA was extracted according to manufacturer recommendations, dissolved in RNase-free water, and further purified by spin cartridge using the PureLink-micro RNA purification system (Invitrogen). Total RNA was dissolved in RNA storage solution (Ambion Life Technology), UV-quantified by a Bio-Photometer (Eppendorf), and stored at −80 °C until use. RNA aliquots (6 μg) were digested by RNase-free DNase I (Ambion DNA-free kit) in a 20-μL final volume reaction mixture to remove residual contaminating genomic DNA. After DNase digestion, concentration and purity of RNA samples were evaluated by the RNA-6000-Nano microchip assay using a 2100 Bioanalyzer equipped with a 2100 Expert Software (Agilent Technology) following the manufacturer's instructions. For all samples tested, the RNA integrity number was greater than 7 relative to a 0–10 scale. One microgram of total RNA, as evaluated by the 2100 Bioanalyzer, was reverse-transcribed in cDNA and analyzed as previously described (3). Optimized primers for SYBR green analysis (GenBank accession nos: Hypocretin Hcrt-NM_010410, hypoxanthine guanine phosphoribosyl transferase Hprt-NM_013556) and optimum annealing temperatures were designed by Allele-Id software version 7.0 (Biosoft International) and were synthesized (HPLC-purification grade) by MWG-Biotech. Relative gene-expression calculation, corrected for PCR efficiency and normalized with respect to the reference gene *Hprt* was performed by the IQ5 software.

Electrophysiology. All of the experiments were performed in acute transverse brain slices that include the lateral hypothalamic area. Miniature inhibitory postsynaptic currents (mIPSCs) were recorded in OX neurons of *ob*/*ob*, their WT siblings and *C57BL/6* mice (*n* of neurons/*n* of mice: 41/18, 33/12, 8/7, respectively). Two developmental stages were investigated: before weaning [3 wk of age, range postnatal day (P)18–P23, average P21], and after weaning (two different ages: 5 wk, P30–P39, average P34, and 9 wk). In a subset of experiments, *ob*/*ob* and WT mice received a single injection of recombinant leptin (5 mg/kg in 100 μL saline, i.p.) 24 h after food withdrawal and the animals were fed ad libitum 24 h before mIPSCs recording (*n* of neurons/*n* of mice: 13/4, 12/4, *ob*/*ob* and WT, respectively). Spontaneous inhibitory postsynaptic currents (sIPSCs) were recorded after weaning (at 5 and 9 wk of age) in 48/21 *ob*/*ob* and 51/35 WT mice (*n* of neurons/*n* of mice). OX neurons in the perifornical hypothalamic area can be functionally identified by their characteristic electrophysiological responses to injected currents (4, 5). These responses are: (*i*) a tonic, nonadapting repetitive spiking evoked in response to a suprathreshold depolarizing pulse; (*ii*) a time- and voltage-dependent rectifying potential change evoked in response to hyperpolarizing pulses; and (*iii*) an abortive spike evoked in response to a subthreshold depolarizing pulse (Fig. S5 *A* and *B*). For our experiments, we selected neurons that showed at least two of the above responses. We further confirmed the validity of the above criteria in a subset of 17 functionally identified neurons that were filled with neurobiotin through the recording electrode and processed with OX-A antibody: only one of these neurons turned out to be nonorexinergic (Fig. S5*C*). With a high concentration of KCl in the recording solution and a holding potential of −70 mV, the chloride-mediated mIPSC and sIPSC appear as an inward current (negative deflection on the recording trace) (Fig. 4*A*). To study depolarization-induced suppression of inhibition (DSI), sIPSC were recorded before and after a step-depolarization (5 s) from −70 to 0 mV. DSI was calculated as the sIPSC frequency measured in time intervals of 5 s after the depolarization and made relative to the frequency during 5 s immediately before the depolarization. In each experiment, the responses to two successive depolarizations (separated by 90 s) were averaged together. In a subset of cells, DSI was also tested 4–5 min after the addition of 4 μM AM. mIPSC and sIPSC frequencies were typically higher at the beginning of each recording and showed a rapid reduction soon after, reaching stable values within 3–4 min. The reduction was similar in *ob*/*ob* and WT neurons and quantified in ∼70% of the initial value (71 ± 6.5%, $n = 9$, 5 *ob*/*ob* and 4 WT pooled together, 9 wk). For this reason, all experiments were performed at least 4 min after the beginning of the recordings, when frequencies were stable, as further demonstrated in a dedicated set of neurons

recorded for an extended period in the presence of DMSO (the AM and WIN55,212-2 vehicle; see *Results*).

Western Blots. Tissue from total hypothalamus or isolated arcuate nucleus (ARC) and LH of mice were homogenized in 1× TNE buffer (50 mM Tris pH 7.4, 150 mM NaCl, 1 mM EDTA) with 1% Triton X-100, protease and phosphatase inhibitor mixtures (Sigma Aldrich). Protein concentrations were analyzed via a Lowryprotein assay (Bio-Rad Laboratories) to allow the loading of the same amount of proteins on SDS/PAGE. Proteins transferred onto PVDF membranes were then blocked in 5% skim milk in TBST (20 mM Tris, 137 mM NaCl, 0.1% Tween-20) and blotted with anti phospho-STAT3 (1:1,000; Santa Cruz Biothechnology), STAT3 (1:1,000; Abcam), p-S6K1 (1:1,000; Cell Signaling), S6K1 (1:1,000; Abcam), phospho-S6RP or S6RP (1:1,000; Cell Signaling) antibodies followed by the appropriate Actb-HRP (1:20,000; Sigma Aldrich) or HRP-conjugated (Bio-Rad Laboratories) secondary antibodies and then detected by ECL (Bio-Rad Laboratories) with autoradiographic film.

Catecholamine and Cortisol Measurements. Blood samples were immediately heparinized, centrifuged at 1,600 × *g* and reconstituted in 0.3 mL of 0.5 M acetic acid solution to obtain the final samples. Plasma catecholamine concentrations were measured by HPLCy and electrochemical detection using an Eicompack CA-50DS column (Eicom). Serum cortisol concentrations were determined by chemioluminescence.

Statistical Analyses. Data are expressed as mean ± SEM. A repeated two-way ANOVA was performed using SPSS version 8.2. Student's or Bonferroni two tail *t* test were used to judge statistical significance between groups.

1. Katona I, et al. (2006) Molecular composition of the endocannabinoid system at glutamatergic synapses. *J Neurosci* 26(21):5628–5637.
2. Marrs WR, et al. (2010) The serine hydrolase ABHD6 controls the accumulation and efficacy of 2-AG at cannabinoid receptors. *Nat Neurosci* 13(8):951–957.
3. Grimaldi P, et al. (2009) The endocannabinoid system and pivotal role of the CB2 receptor in mouse spermatogenesis. *Proc Natl Acad Sci USA* 106(27):11131–11136.
4. Eggermann E, et al. (2003) The wake-promoting hypocretin-orexin neurons are in an intrinsic state of membrane depolarization. *J Neurosci* 23(5):1557–1562.
5. Li Y, Gao XB, Sakurai T, van den Pol AN (2002) Hypocretin/Orexin excites hypocretin neurons via a local glutamate neuron-A potential mechanism for orchestrating the hypothalamic arousal system. *Neuron* 36(6):1169–1181.

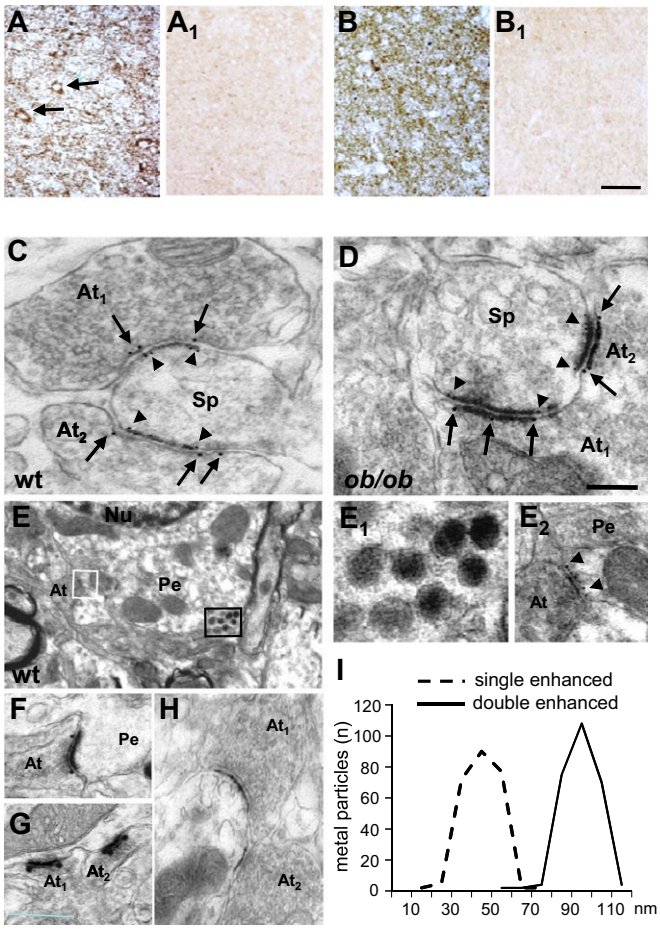

Fig. S1. Additional data of the endocannabinoid system at orexin neurons. (*A*) DAGLα immunoreactivity in puncta with a perisomatic distribution (arrows) and in the LH neuropil. (*A1*) Control of DAGLα specificity by blank labeling in DAGLα-KO mice. (*B*) MAGL immunoreactivity in the LH neuropil. (*B1*) Control of MAGL specificity by blank labeling in MAGL-KO mice. (Scale bar, 100 μm.) (*C–E*) Representative electron micrographs showing double OX/DAGLα or CB_1R/DAGLα or OX/CB_1R immunogold detection by preembedding of 6-nm and 10-nm metal particles in 9-wk-old WT and *ob/ob* mice. (*C*) Asymmetrical, putative excitatory, axodendritic synapses in the LH of WT mice with 6-nm DAGLα gold particles at postsynaptic membrane specialization of a dendritic spine (Sp; arrowheads). Ten-nanometer CB_1R particles are located in two different axon terminals (At1 and At2, arrows) at the edges of each presynaptic site, opposite to DAGLα. (*D*) Symmetrical, putative inhibitory, axodendritic synapse in the LH of *ob/ob* mice showing 6-nm DAGLα and 10-nm CB_1R particles distributed as in *C*. (*E*) Six-nanometer DAGLα gold particles are confined to the postsynaptic side, close to the cell membrane (white boxed area) of an OX neuron containing 10-nm OX gold particles clustered in large dots within dense cytosolic vesicles (black boxed area). (E_1) Higher magnification of the black boxed area showing clusters of OX gold particles. (E_2) Higher magnification of the white boxed area showing 6-nm DAGLα gold particles (arrowheads). (*F* and *G*) Control of gold particle size following single (*F*) vs. double (*G*) silver enhancement of the secondary antibody to visualize CB_1R. Enhancing one of the gold labels twice vs. once resulted in approximately doubling of its size. (*H*) Control of antibody specificity obtained by omitting the mixture of primary antibodies. Note the absence of gold particle deposition. At, axonal terminal; Nu, nucleus; Pe, perikaryon, Sp, dendritic spine. (Scale bar: 0.1 μm for *C* and *D*; 1.4 μm for *E*; 0.2 μm for E_1; 0.12 μm for E_2; 0.3 μm for *F*; 0.6 μm for *G* and *H*). (*I*) Gaussian distribution of metal particle size ($n = 250$ particles) for CB_1R immunolabeling obtained by single vs. double silver enhancement.

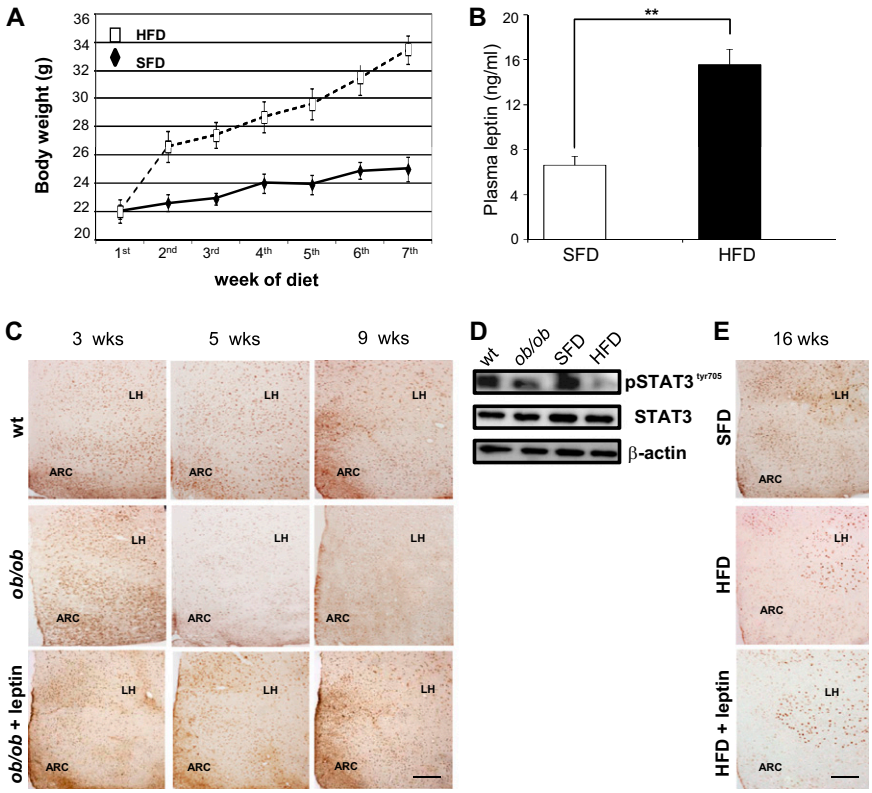

Fig. S2. Obesity-inducing effect of HFD in mice and its effect on leptin sensitivity. (*A*) Time course profile of body weight increase in mice fed with either a SFD or HFD for 7 wk, starting from the ninth week of age. (*B*) Analysis of leptin plasma levels after the seventh week of SFD or HFD. $n = 20$ mice per group; mean ± SEM; $^{**}P < 0.01$. (*C*) Leptin-stimulated STAT3 posphorylation (pSTAT3) in the hypothalamus. Representative hypothalamic sections collected from 3-wk-old (preweaned), 5-wk-old (weaned), and 9-wk-old *ob/ob* and WT mice showing lack of pSTAT3 immunostaining in both the ARC and LH of *ob/ob* mice after weaning compared with WT or leptin-injected (5 mg/kg, i.p.) *ob/ob* mice of the same age. (Scale bar, 200 μm.) (*D*) Representative Western blot analysis of pSTAT3 in the whole hypothalamus of adult *ob/ob* mice and WT littermates, and HFD mice and matched SFD controls. (*E*) pSTAT3 immunostaining through the hypothalamus of HFD mice and matched SFD mice show selective lack of immunostaining in the ARC of HFD mice and HFD leptin-injected mice. (Scale bar, 200 μm.)

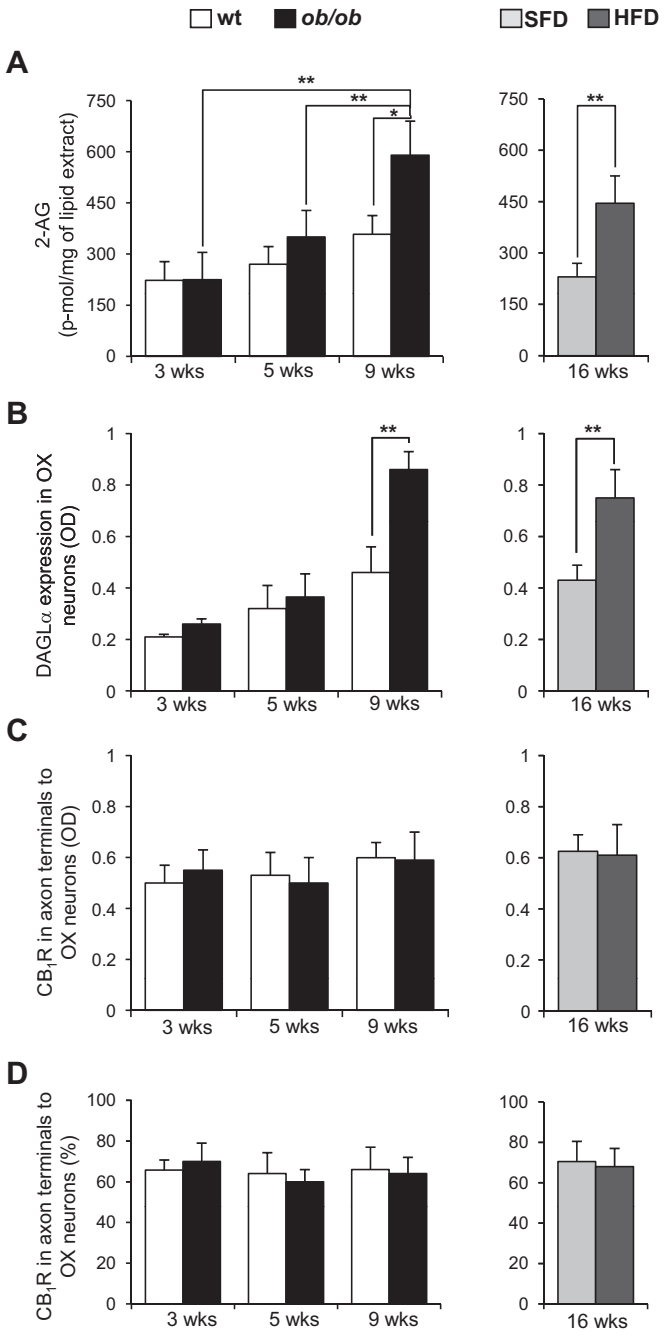

Fig. S3. Levels of DAGLα protein and 2-AG in the LH increase during obesity. (*A*) The 2-AG levels were evaluated by LC-MS on the LH isolated from the brain of mice of all groups. Data are mean ± SD, $n = 3$ mice per group. (*B*) Densitometric analysis of DAGLα immunosignal (optical density, OD) performed on OX neurons identified on adjacent sections processed for DAGLα/OX immunoreactivity. (*C*) Densitometric analysis of CB_1R immunoreactivity in axon terminals apposed to OX neurons. (*D*) Percentage of CB_1R-expressing axon terminals to OX neurons. Data are mean ± SEM, $n = 500$ OX neurons per group; $n = 3$ mice per group. $^*P < 0.05$; $^{**}P < 0.01$.

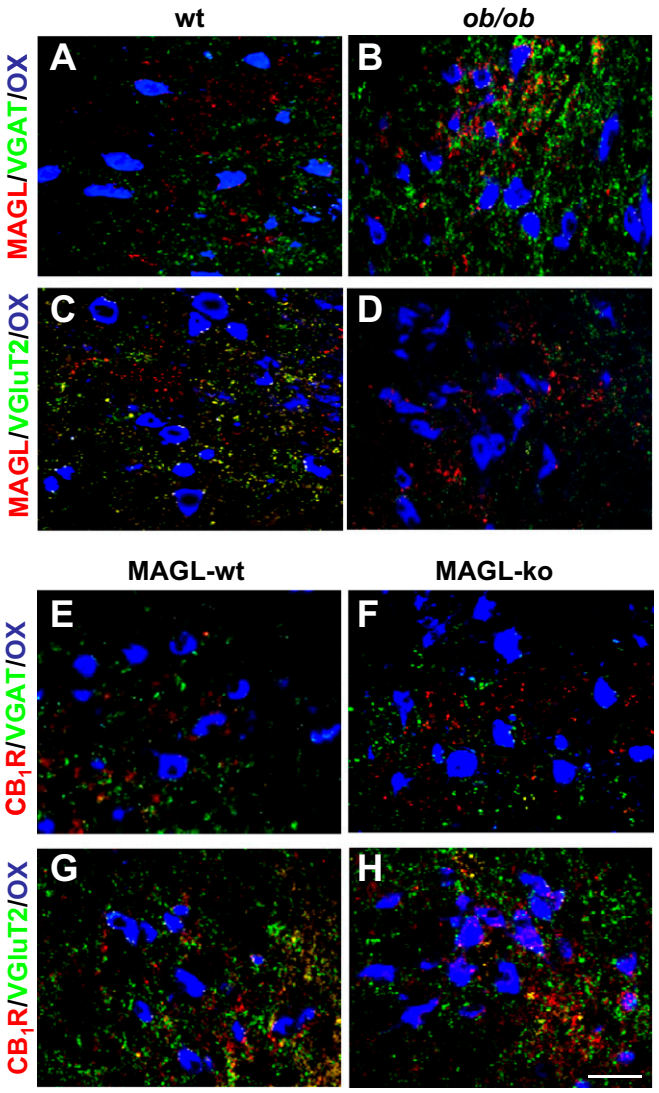

Fig. S4. MAGL–expressing fibers innervating OX neurons are rearranged in *ob/ob* mice. (*A–D*) Representative images of MAGL/VGAT- vs. MAGL/VGluT2-expressing axon terminals apposed to OX neurons of adult *ob/ob vs*. WT mice, showing the prevalence of MAGL/VGluT2 puncta in WT and the prevalence of MAGL/VGAT puncta in *ob/ob* mice. CB_1-expressing fibers innervating OX neurons are not rearranged in MAGL-KO mice. (*E–H*) Prevalence of CB_1R/VGluT2-expressing over CB_1R/VGAT-expressing axon terminals apposed to OX neurons in both WT and MAGL-KO mice. (Scale bar, 50 μm.)

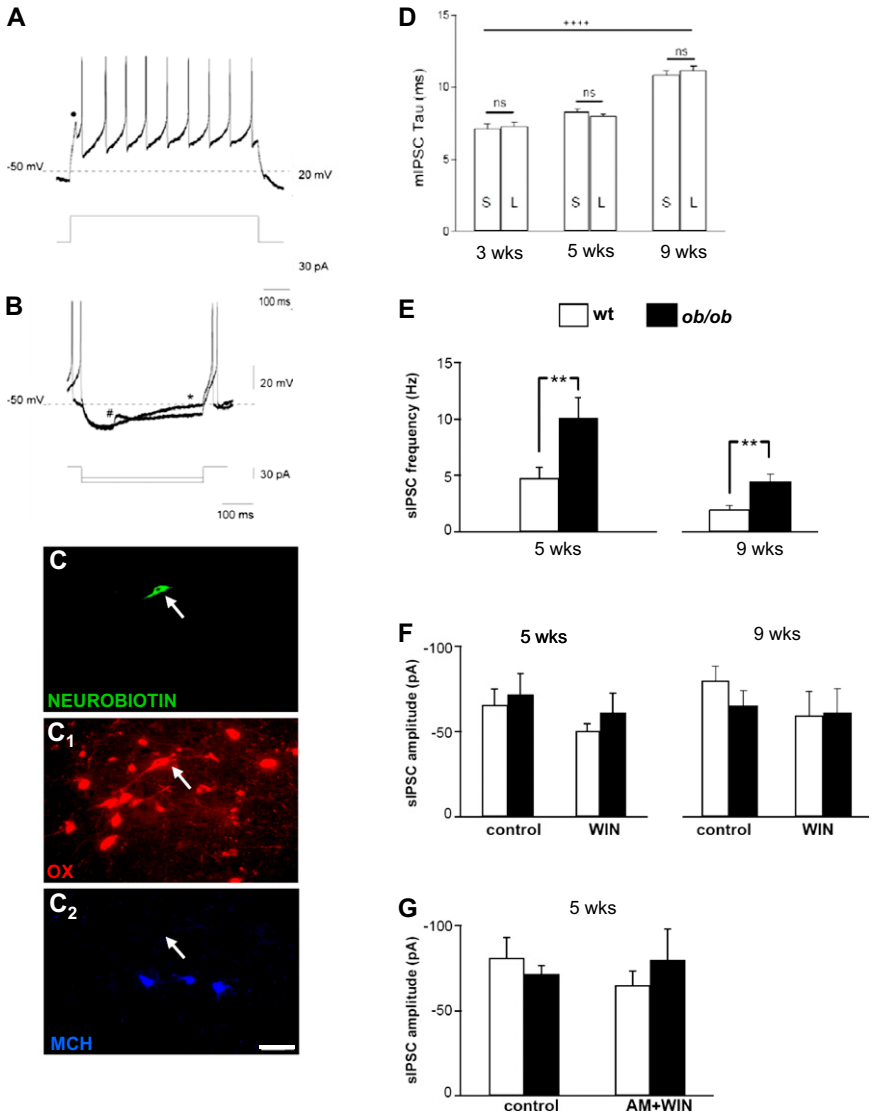

Fig. S5. Criteria used to identify OX neurons and additional data on mIPSC and sIPSC. Intrinsic membrane properties of OX neurons that allow their functional identification within the LH neurons. (*A*) representative voltage recording of an abortive spike (black dot) and the tonic nonadapting firing in response to a depolarizing current pulse (65 pA) delivered from a slightly hyperpolarized potential (resting membrane potential is indicated by the dotted line) obtained through injected DC current. (*B*) Two superimposed representative voltage recordings both characterized by a sag (*) indicative of a time- and voltage-dependent membrane rectification in response to hyperpolarizing current pulses (30 and 35 pA) delivered from a slightly depolarized potential. One trace shows also a spontaneous inhibitory postsynaptic potential (#), which has a depolarizing nature because of the recording conditions (see *SI Materials and Methods*). (*C*) Example of the immunohistochemical identification of an OX neuron (arrow) filled with neurobiotin through the recording electrode and functionally identified as OX on the basis of its electrophysiological properties. The neuron is OX-immunoreactive and MCH-immunonegative. (Scale bar, 50 μm.) (*D*) Equal inactivation kinetics of mIPSCs of same age. For each age, mIPSC are sorted by amplitude and divided in two groups of equal number of events, one group including mIPSCs of small amplitude (S) and the other group with mIPSCs of large amplitude (L). Shown are the mean ± SEM of decaying τ values. No difference (ns) is observed for individual comparisons. ANOVA reveals a general trend toward longer τ values in older animals (++++ $P < 0.00001$, ANOVA). (*E*) Higher sIPSC frequency in *ob/ob* compared with WT OX neurons (5 wk: *ob/ob* 10.0 ± 1.9 Hz, $n = 29$, WT: 4.8 ± 0.94 Hz, $n = 37$; 9 wk: *ob/ob* 4.4 ± 0.72 Hz, $n = 15$, WT: 1.9 ± 0.36 Hz, $n = 13$). **$P < 0.01$. (*F*) WIN does not modify sIPSC amplitude [pre- (control) and post-WIN at 5 wk: *ob/ob* −71 ± 12.5 and −61 ± 11.2 pA, $n = 9$, $P > 0.1$; WT: −66 ± 9.3 and −50 ± 4.4 pA, $n = 9$, $P > 0.05$; pre- (control) and post-WIN at 9 wk: ob/ob −65 ± 8.6 and −61 ± 13.8 pA, $n = 7$, $P > 0.5$; WT: −79 ± 13.7 and −60 ± 15.1 pA, $n = 8$, $P > 0.05$]. (*G*) AM+WIN does not affect sIPSCs amplitude [pre- (control) and post-AM+WIN: *ob/ob* −71 ± 12.5 and −80 ± 18.0 pA, $n = 6$, $P > 0.1$; WT −81 ± 12.0 and −65 ± 8.5 pA, $n = 4$, $P > 0.5$. Recordings performed at 5 wk]. Data are expressed as mean ± SEM.

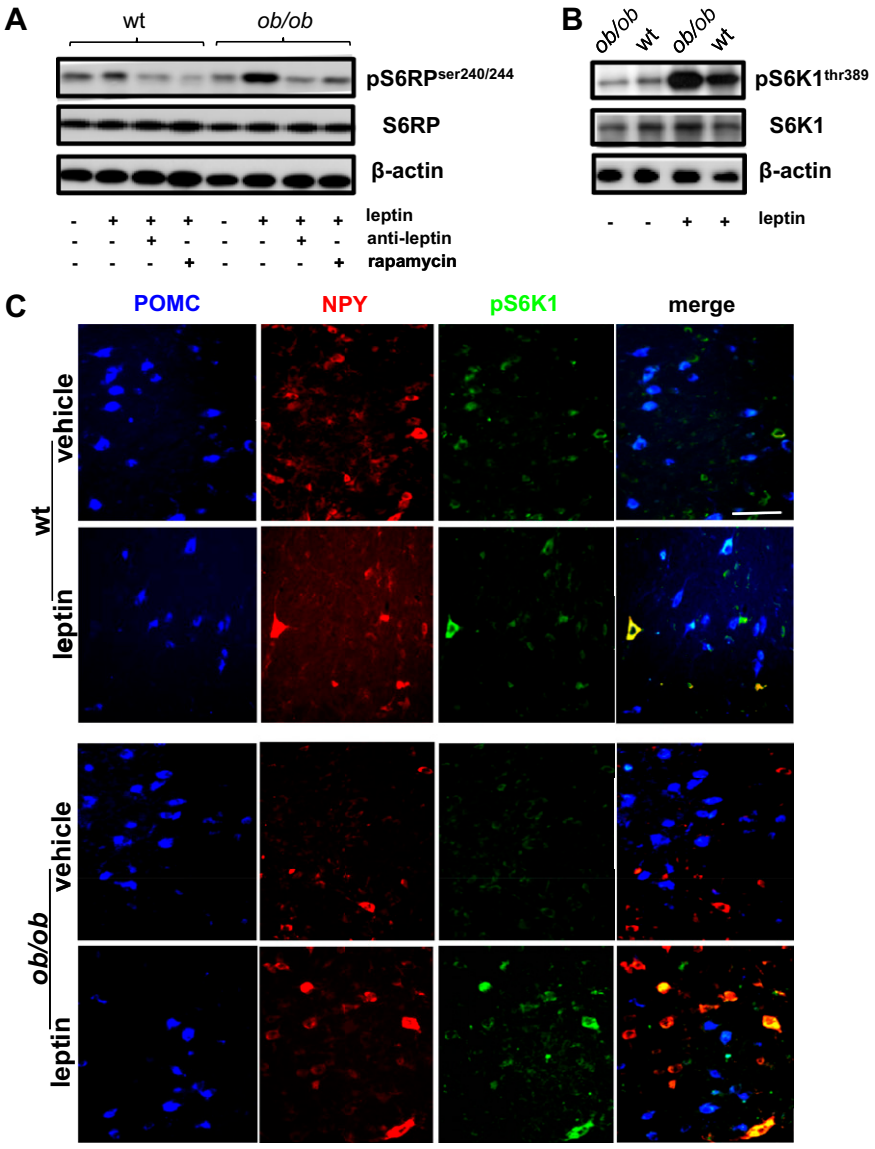

Fig. S6. Localization of mTOR signaling components in the ARC of obese mice and matched controls. (*A*) Representative Western blot analysis of pS6RP and total S6RP from the ARC of WT or *ob/ob* mice treated with vehicle or leptin for 24 h plus fasting, with or without previous injection of leptin receptor antagonist ("anti-leptin") or rapamycin. (*B*) Representative Western blot analysis of pS6K1 and total S6K1 from the ARC of WT or *ob/ob* mice treated with leptin for 24 h plus fasting. (*C*) Representative immunofluorescence showing the presence of pS6K1 in several NPY neurons and some POMC neurons in the ARC of WT mice. Leptin treatment enhances and induces the pS6K1 signal in wt and *ob/ob* mice, respectively. (Scale bar, 100 μm.)

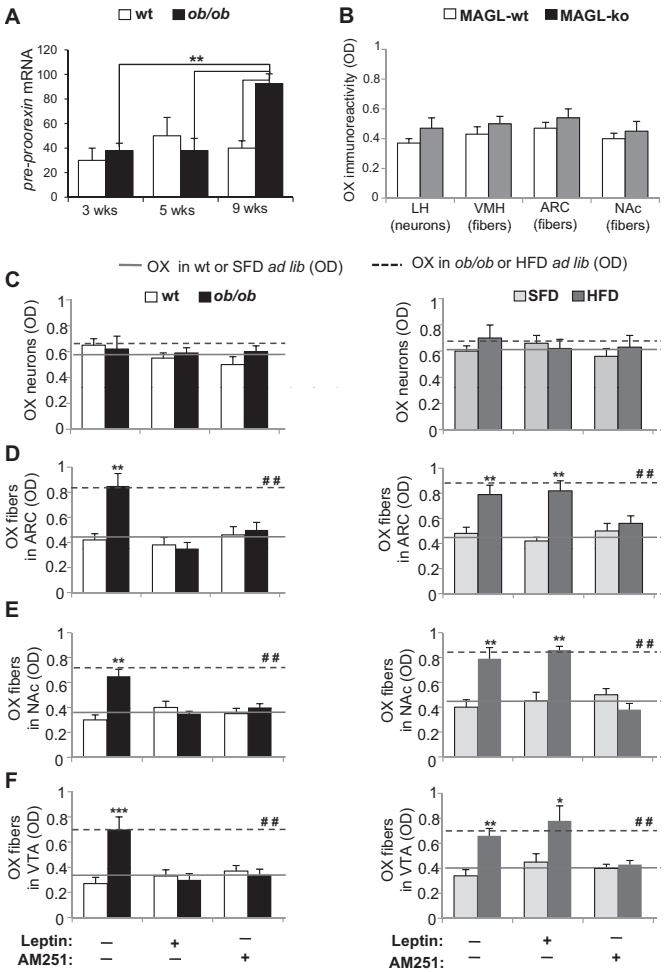

Fig. S7. Increase of OX expression in preterminal and terminal fibers innervating the ARC, nucleus accumbens (NAc) and ventral tegmental (VTA) areas in obese mice. (*A*) *Preproorexin* mRNA expression increases significantly in the LH of 9-wk-old *ob/ob* mice. (*B*) No change in the intensity of OX immunosignal was detected in OX cell bodies or OX fibers innervating the ARC, NAc, and ventral medial hypothalamus (VMH) of MAGL-WT and MAGL-ko mice. (*C*) Optical density (OD units) of OX immunostaining in cell bodies ($n = 300 \pm 20$ OX neurons per group, $n = 3$ mice per group) and fibers projecting to ARC (*D*), NAc (*E*), and VTA (*F*) of 24 h fasted, lean (WT and SFD) mice and obese (*ob/ob* and HFD) littermates or in lean (solid lines) and obese (dotted lines) mice fed ad libitum. $n = 3$ mice per group. Data are mean ± SEM; $n = 3$ mice per group; $^{*}P < 0.05$; $^{**}P < 0.001$; $^{***}P < 0.0001$; $^{\#\#}P < 0.001$ vs. solid lines.

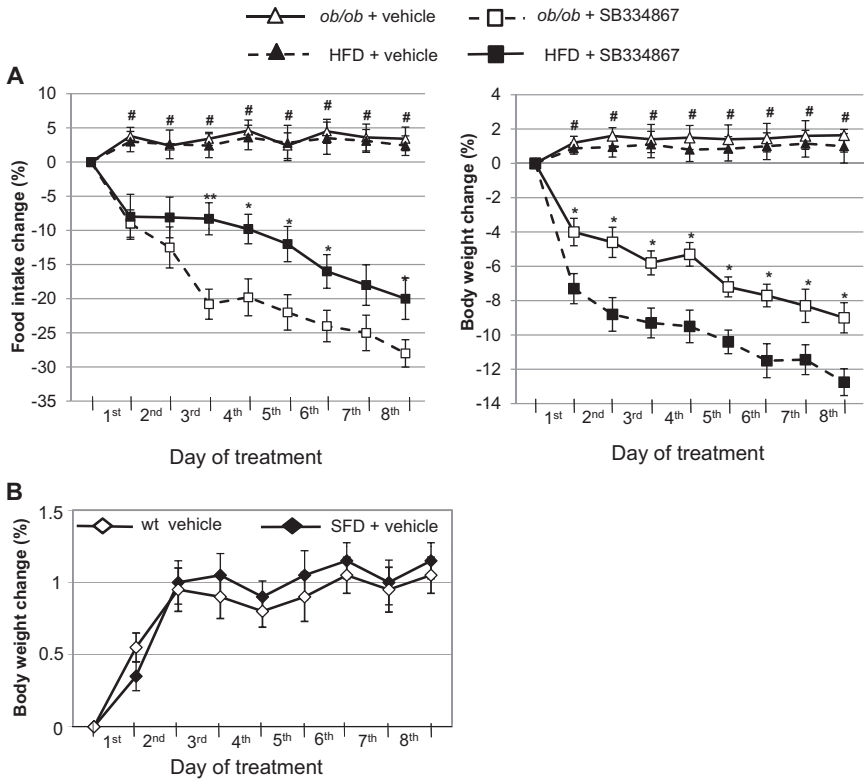

Fig. S8. Effect of systemic administration of OX receptor antagonist on daily food intake and body weight. (*A*) The OX receptor antagonist SB-334867 reduces daily food intake and body weight in adult *ob/ob* and HFD obese mice with respect to vehicle-injected matched obese mice. (*B*) Percentage of body weight change in WT and SFD lean vehicle-injected mice. Data are mean ± SEM of $n = 5$ mice per group; $^{\#}P < 0.05$ for vehicle-injected vs. SB-334867-injected mice.$^{*}P < 0.05$; $^{**}P < 0.001$ for *ob/ob* vs. HFD mice treated with the antagonist. The body weight of obese *ob/ob* and HFD mice (*ob/ob*: 42 ± 6 g and HFD: 39 ± 4 g), and of lean WT and SFD mice (WT: 22 ± 3 g and SFD: 20 ± 2 g) was similar at the beginning of treatment.